Osteogenic and antibacterial surfaces on additively manufactured porous Ti-6Al-4V implants

Combining silver nanoparticles with hydrothermally synthesized HA nanocrystals

Fazel, Mohammad; Salimijazi, Hamid R.; Shamanian, Morteza; Minneboo, Michelle; Modaresifar, Khashayar; van Hengel, Ingmar A.J.; Fratila-Apachitei, Lidy E.; Apachitei, Iulian; Zadpoor, Amir A.

DOI
10.1016/j.msec.2020.111745

Publication date
2021

Document Version
Final published version

Published in
Materials Science and Engineering C

Materials Science & Engineering C 120 (2021) 111745

Contents lists available at ScienceDirect

Materials Science & Engineering C

journal homepage: www.elsevier.com/locate/msec

Osteogenic and antibacterial surfaces on additively manufactured porous Ti-6Al-4V implants: Combining silver nanoparticles with hydrothermally synthesized HA nanocrystals

Mohammad Fazel [a,b,*], Hamid R. Salimijazi [b], Morteza Shamanian [b], Michelle Minneboo [a], Khashayar Modaresifar [a], Ingmar A.J. van Hengel [a], Lidy E. Fratila-Apachitei [a], Iulian Apachitei [a], Amir A. Zadpoor [a]

[a] Department of Biomechanical Engineering, Delft University of Technology, Mekelweg 2, 2628 CD Delft, the Netherlands
[b] Department of Materials Engineering, Isfahan University of Technology, Isfahan 84156-83111, Iran

ARTICLE INFO

Keywords:
Additively manufacturing
Plasma electrolytic oxidation
Hydrothermal treatment
Hierarchical structure
Hydroxyapatite nanocrystals
Multifunctional surfaces

ABSTRACT

The recently developed additively manufacturing techniques have enabled the fabrication of porous biomaterials that mimic the characteristics of the native bone, thereby avoiding stress shielding and facilitating bony ingrowth. However, aseptic loosening and bacterial infection, as the leading causes of implant failure, need to be further addressed through surface biofunctionalization. Here, we used a combination of (1) plasma electrolytic oxidation (PEO) using Ca-, P-, and silver nanoparticle-rich electrolytes and (2) post-PEO hydrothermal treatments (HT) to furnish additively manufactured Ti-6Al-4V porous implants with a multi-functional surface. The applied HT led to the formation of hydroxyapatite (HA) nanocrystals throughout the oxide layer. This process was controlled by the supersaturation of Ca^{2+} and PO_4^{3-} during the hydrothermal process. Initially, the high local supersaturation resulted in homogenous nucleation of spindle-like nanocrystals throughout the surface. As the process continued, the depletion of reactant ions in the outermost surface layer led to a remarkable decrease in the supersaturation degrees. High aspect-ratio nanorods and hexagonal nanopillars were, therefore, created. The unique hierarchical structure of the microporous PEO layer (pore size < 3 μm) and spindle-like HA nanocrystals (<150 nm) on the surface of macro-porous additively manufactured Ti-6Al-4V implants provided a favorable substrate for the anchorage of cytoplasmic extensions assisting cell attachment and migration on the surface. The results of our *in vitro* assays clearly showed the important benefits of the HT and the spindle-like HA nanocrystals including a significantly stronger and much more sustained antibacterial activity, significantly higher levels of pre-osteoblasts metabolic activity, and significantly higher levels of alkaline phosphatase activity as compared to similar PEO-treated implants lacking the HT.

1. Introduction

Thanks to a number of properties, such as good corrosion resistance, high strength to weight ratio, and relatively low modulus of elasticity, titanium and its alloys are among the most attractive metallic biomaterials for dental and orthopedic applications [1,2]. There is, nevertheless, a mismatch between the elastic modulus of bone and that of the implant [3], which might lead to stress shielding and, thus, bone resorption, eventually resulting in aseptic loosening [4,5] or bone fracture [6,7]. To address the issues associated with such a mismatch while providing a fully interconnected porous structure that supports bone tissue regeneration and bony ingrowth, researchers have been trying to develop porous metallic biomaterials. While the initial attempts using conventional manufacturing techniques [8] have been only partially successful, the recent developments in the field of additive manufacturing have provided unprecedented opportunities for the fabrication of rationally designed porous implants with the desired mechanical properties [9,10]. Indeed, not only the mechanical properties and the porous structure, but also permeability [11,12], fatigue behavior [13,14], surface area [15,16], and many other properties of such additively manufactured porous structures can be adjusted through the application of (advanced) geometrical designs.

* Corresponding author at: Department of Biomechanical Engineering, Delft University of Technology, Mekelweg 2, 2628 CD Delft, the Netherlands.
E-mail address: mohammad.fazel@ma.iut.ac.ir (M. Fazel).

https://doi.org/10.1016/j.msec.2020.111745
Received 18 June 2020; Received in revised form 13 October 2020; Accepted 18 November 2020
Available online 26 November 2020

Despite all the advantages offered by an optimum geometrical design, it cannot address all the challenges associated with orthopedic implants. The surface properties of the biomaterial should be also optimized to promote the adhesion, proliferation, and osteogenic differentiation of host cells while preventing bacteria adhesion and implant-associated infections (IAIs) [17,18]. Creating such a differential behavior against two types of cells is particularly challenging and requires the application of multi-functional coatings that are carefully designed to have opposite effects on the host and bacterial cells. When applied properly, a multi-functional coating could enable the host cells to win the '*race for the surface*' [19], which is an early post-surgery contest between the host cells and bacteria to colonize the implant surface. If the race is won by bacteria, they can rapidly form a biofilm on the implant surface, leading to periprosthetic joint infections while impairing the osseointegration of the implant. The biofilm is believed to form a protective shield against antibacterial agents, rendering the systemic antibiotic treatments ineffective [20].

Here, we report a novel multi-functional layer on additively manufactured Ti-6Al-4V porous implants. The layer combines silver nanoparticles (Ag NPs) with hydrothermally synthesized HA nanocrystals. Silver nanoparticles incorporated onto the layer release silver ions that are very potent antibacterial agents against a wide spectrum of pathogens. Furthermore, resistance against silver is extremely rare and difficult to obtain by bacteria [21]. Finally, silver nanoparticles are very stable, thereby allowing for their incorporation into coatings using a variety of techniques while lasting for many years and providing long-term protection against IAIs. However, silver could also adversely affect host cell viability and retard the proliferation of osteogenic cells [22–25].

An ideal antimicrobial implant surface is, therefore, believed to need tightly immobilized Ag NPs on the surface to gradually release silver ions in the surrounding tissue. Croes et al. [23] used electrophoretic deposition (EPD) to create chitosan-based coatings with incorporated silver nanoparticles and prevent IAI. According to their results, despite the high efficiency of silver against bacteria colonization, the antibacterial EPD coatings were found to negatively affect both bone and phagocytic cells response. On the other hand, the commonly used line-of-sight techniques, such as plasma spraying are technically inapplicable in the surface modification of complex additively manufactured structures [25–27]. We, therefore, used plasma electrolytic oxidation (PEO), which is capable of embedding nanoparticles from the electrolyte into the oxide matrix. Another advantage of PEO treatment is that the chemical composition of the oxide layer can be governed by the incorporation of calcium and phosphate species from the electrolyte [28–30]. These species mainly remain as dissolved ions or amorphous phases within the PEO layer [1,30,31]. However, a sufficient concentration of Ca and P in the outermost surface of the PEO layers can enable formation of hydroxyapatite (HA) [32,33]. We, therefore, aimed to produce HA nanocrystals through a post-PEO hydrothermal treatment applied to 3D porous additively manufactured Ti-6Al-4V implants after they were firstly surface-modified by PEO in Ca/P based electrolytes containing Ag NPs. Subsequently, the effects of such a layer on the response of pre-osteoblasts and bacteria cells were studied.

2. Materials and methods

2.1. Additive manufacturing and surface bio-functionalization

Porous implants designed for implantation in a mouse femur model [15] were used as the substrate materials in this study. To manufacture the implants by selective laser melting (SLM), which is a powder-based layer-by-layer additive manufacturing technique, spherical grade-23 Ti-6Al-4V powder (AP&C, Canada) with a size distribution of 10–40 μm were used. To remove the excess powder particles after printing, the implants were ultrasonically cleaned with acetone, ethanol, and demineralized water, consecutively.

The PEO process was performed using a custom-made AC power supply (type ACS 1500, ET Power Systems Ltd., UK) in an aqueous electrolyte containing 0.15 M calcium acetate, 0.02 M calcium glycerophosphate, and 2 g/l silver nanoparticles (Sigma-Aldrich, St. Louis, Missouri, United States) where the porous implant was used as an anode while a stainless steel plate was used as the cathode. The applied current density, frequency, and oxidation time were set to 20 A/dm^2, 50 Hz, and 5 min, respectively.

For hydrothermal treatment, the PEO-treated samples (SLM-PEO) were vertically suspended in a Teflon-lined autoclave containing 300 ml of distilled water. The specimens were autoclaved at 250 °C for 2 (SLM-PEO-HT2) and 4 (SLM-PEO-HT4) hours and were thereafter rinsed with distilled water and dried with warm air.

2.2. Surface characterization

The surface morphology and chemical composition of the PEO and PEO-HT treated specimens were examined using a field emission scanning electron microscope equipped with an energy-dispersive X-ray spectroscope (FESEM; FEI Helios G4 CX and JEOL JSM-6500F).

X-ray diffraction profiles were determined using a Bruker D8 Advance diffractometer employing Cu K_α radiation (45 kV and 40 mA) at brag angles of 10–110°.

The static release of calcium and silver ions from the different groups of surface-treated implants was evaluated using inductively coupled plasma-optical emission spectrometry (ICP-OES) with a PerkinElmer Optima 3000DV (PerkinElmer, Zaventem, Belgium). Toward that end, three specimens from each group were submerged in 1 ml of phosphate-buffered saline (PBS) that was kept at 37 ± 0.5 °C. The entire volume was sampled and replaced by 1 ml of fresh PBS at specific time points (*i.e.*, 1, 3, 5, 7, and 15 days) to measure the concentration of calcium and silver ions. The measurements were repeated three times for each time point.

2.3. Cell response

Multiple implants from each experimental group (length = 1 cm) were sterilized by autoclaving at 110 °C for 20 min. Preosteoblast MC3T3-E1 cells (Sigma-Aldrich) were maintained in a standard culture medium containing α-minimum essential medium (α-MEM; no ascorbic acid, Thermo Fisher, United States), supplemented with 10% fetal bovine serum (FBS; Thermo Fisher, United States) and 1% PenStrep (Thermo Fisher, United States). Each implant was seeded with 100 μl cell suspension containing 150,000 cells and the samples were flipped once per 20 min during the first 2 h of incubation. After the incubation, the samples were transferred into a well plate. Cell differentiation was induced after 2 days using an osteogenic medium (*i.e.*, the standard culture medium with 50 μg/ml ascorbic acid (Sigma-Aldrich A4403, The Netherlands) and 4 mM β-glycerophosphate (Sigma-Aldrich G9422, The Netherlands)). The medium was refreshed every 2 days. The PrestoBlue assay was used to assess the metabolic activity of cells on SLM-PEO, SLM-PEO-HT2, and SLM-PEO-HT4 implants (n = 4/group). On days 1, 4, 7, and 14, the samples were transferred to a new well and the PrestoBlue reagent was added to each well (10% vol.). The plates were further incubated at 37 °C for 1 h. The absorbance (λ = 595 nm) of each well was finally measured using a Victor X3 microplate reader (Perkin Elmer, The Netherlands).

To study the morphology of the cells on days 1, 7, and 14 of the cell culture experiments, the specimens (n = 2/group) were fixated with 1% glutaraldehyde and 4% Paraformaldehyde and were dehydrated. The surfaces were then gold-sputtered and examined by FESEM (FEI Helios G4 CX).

The osteogenic differentiation of the cells was assessed by measuring the alkaline phosphate (ALP) activity (n = 3/group). Following 7 and 14 days of culture, the implants were rinsed with PBS and submerged in 250 μl of PBS/Triton (0.1% Triton X-100 in 1× PBS). The implants were

then sonicated for 10 s and incubated at 37 °C with 100 μL para-nitrophenylphosphate (p-NPP, Sigma-Aldrich). After 10 min, the reaction was stopped by adding 250 ml NaOH. The absorbance was then measured at a wavelength of 405 nm using a Victor X3 microplate reader (Perkin Elmer, The Netherlands). The absorbance results were quantified by comparison with a standard sample, which was prepared by the addition of 100 ml PBS-Triton and 250 ml NaOH to each well. The total protein content was also measured by the bicinchoninic acid (BCA) protein assay (Thermo Fisher Scientific, The Netherlands). The amount of ALP was, then, normalized to the level of the total protein content.

2.4. Antibacterial assays

Staphylococcus aureus (*S. aureus*) (RN0450 strain, BEI Resources, United States) was grown on brain heart infusion (BHI) (Sigma-Aldrich, United States) agar plates and a single bacterial colony was used to prepare a bacterial suspension in BHI broth (Sigma-Aldrich, United States) as previously described [34]. Bacterial cells were collected at their logarithmic stage of growth and the optical density of the final suspension was adjusted to a value of 0.1 (equivalent to 55×10^6 CFU/ml), measured by a WPA Biowave II spectrophotometer (Biochrom, UK). The specimens were then submerged in tubes containing 200 μl of the bacterial suspension and were incubated at 37 °C for 48 h.

The PrestoBlue assay was carried out to measure the metabolic activity of the bacteria adhered to the implant as an indicator of their viability [35]. After 4 h of culture, the specimens were rinsed with the phosphate buffer saline (PBS) solution to remove non-adherent bacteria and were then transferred to new tubes, were supplied with 180 μl of BHI broth and 20 μl of PrestoBlue reagent (Thermo Fisher, United States), and were incubated at 37 °C for 1 h. Subsequently, 100 ml of the medium from each tube was added to a 96-well plate (in duplicate) and its absorbance was measured at a wavelength of 595 nm using a Synergy 2 microplate reader (BioTek, United States). This procedure was repeated at 8, 24, and 48 h of bacterial culture to reveal the viability of the adhered bacteria over time.

Further evaluation was conducted by SEM imaging. Briefly, the bacterial cells adhered to the surface of the implants were fixated by a solution containing 4% formaldehyde (Sigma-Aldrich, United States) and 1% glutaraldehyde (Sigma-Aldrich, United States) in 10 mM PBS. The specimens were dehydrated prior to their imaging through a series of washing by ultrapure water, 50%, 70%, and 96% ethanol, and followed by air-drying. The samples were then sputter-coated with a layer of gold and imaged by SEM (Philips XL 30, The Netherlands).

3. Results and discussion

3.1. Surface characterization and thickness measurements

The single-step PEO treatment endowed the surfaces of the macro-porous 3D-printed implants with small pores, ranging from a few nanometers up to about 3 μm in size (Fig. 1). These micropores have been reported to play an important role in creating a stronger bonding between the bone tissue and implant surfaces [26]. Moreover, the PEO process had little effect on the macro-porous architecture of the 3D-printed specimens.

During the initial seconds of the PEO treatment and under galvanostatic conditions, the voltage linearly increased with time to keep the electric field constant across the oxide layer (Stage I, Fig. 2a). Similar to anodic oxidation, this stage results in the formation of a thin and compact oxide film [36]. As the thickness of the oxide layer reached a critical value, the anodic voltage exceeded the dielectric breakdown limit of the oxide layer. After the so-called breakdown potential, the rate of the increase in the voltage decreased (Stage II, Fig. 2a) with the current flow being concentrated at the discharge points. This stage was characterized by gas emission and a large number of short-lived sparks quickly moving over the implant surface, indicating the continuous formation and breakdown of the oxide layer. As the oxidation process continued, the discharge sparks grew larger, accompanied by slight oscillations in the voltage (Stage III, Fig. 2a). According to Hussein et al. [37], the plasma temperature in this stage is high enough to excite the

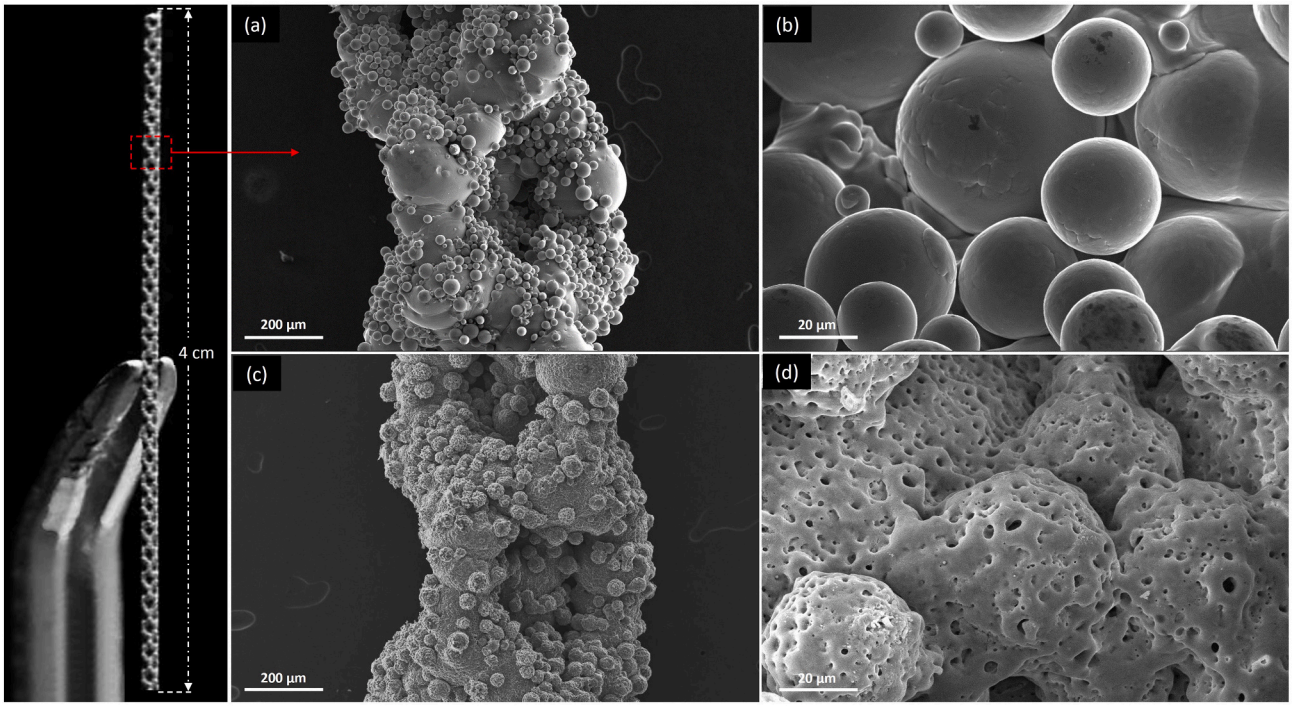

Fig. 1. The macro-scale view and the SEM micrographs of the additively manufactured Ti-6Al-4V implants. (a) The surface morphology of the as-printed SLM implant after particle removal, (b) partially molten Ti-6Al-4V particles on the implant surface, (c, d) the hybrid macro-micro porous structure of the PEO-treated implants revealing the uniform oxidation of the entire surface including fully/partially molten particles.

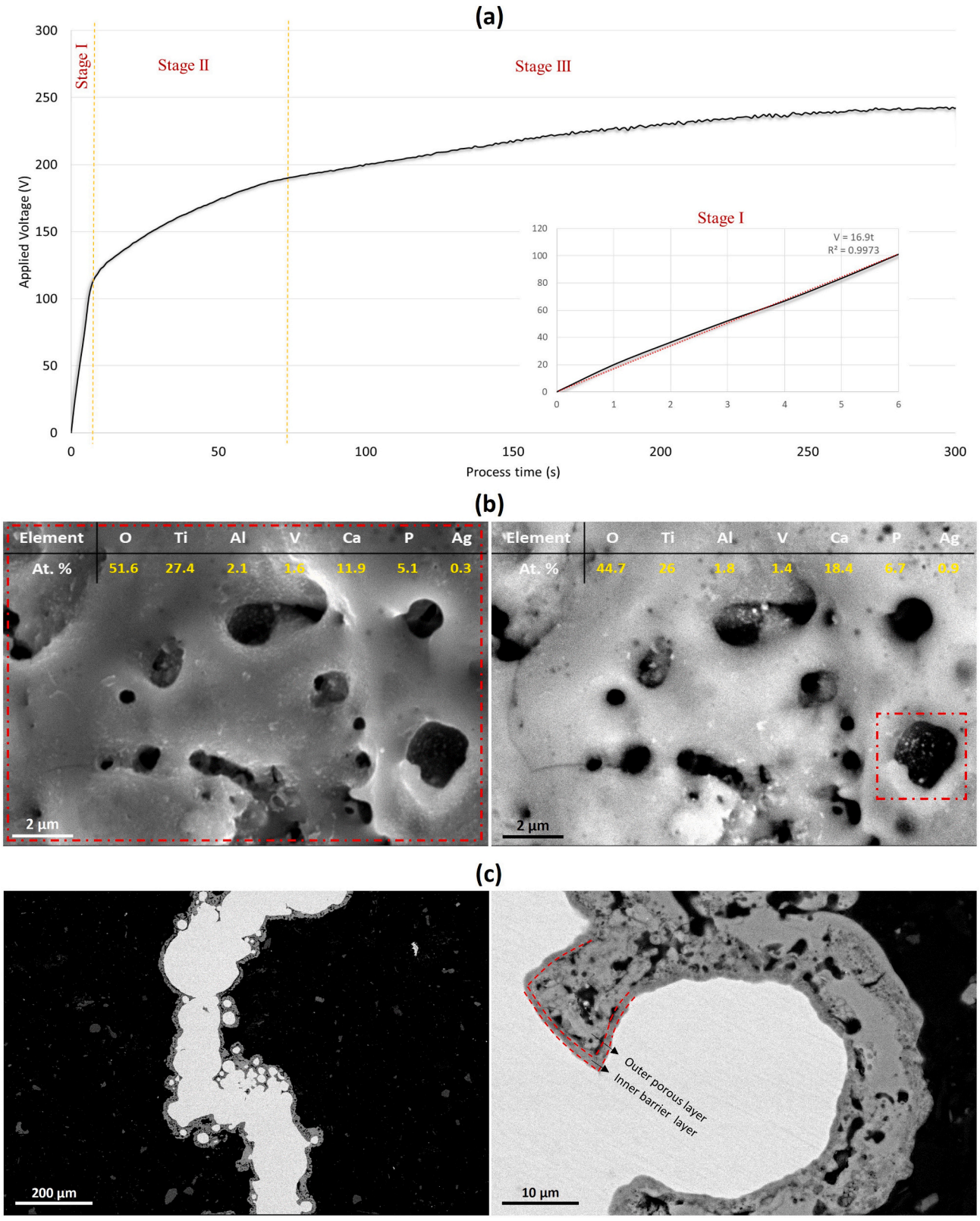

Fig. 2. (a) The PEO voltage transients of SLM implants in an electrolyte containing 2 g/l Ag NPs at 20 A/dm^2 for 5 min. (b) The SE and BSE SEM images of the Ag-containing PEO-treated implants reveal the presence of Ag NPs on the surface and inside the porosities. The EDS analysis confirmed the presence of Ag NPs. (c) A cross-sectional SEM image of a PEO-treated implant. The presence of both an inner dense layer and an outer porous layer can be observed on a partially molten particle.

ionic species and nanoparticles in the electrolyte. The EDS analysis revealed that a significant concentration of Ca and P was successfully incorporated onto the surface of the PEO-treated specimens (Fig. 2b).

The high energy micro-arcs also caused localized melt channels in the oxide layer. Erupted molten materials, in contact with the surrounding electrolytic solution, rapidly solidified around the top of the craters, creating large and protruding pores. The nanoparticles adsorbed onto the surface could, therefore, be embedded within the TiO_2 matrix as well as on the implant surface. This is consistent with BSE-SEM images (Fig. 2b), where Ag NPs were found inside the pores and around the discharge channels. The higher concentration of Ca and P in the EDS spectrum around the pores confirmed that both the ionic species and

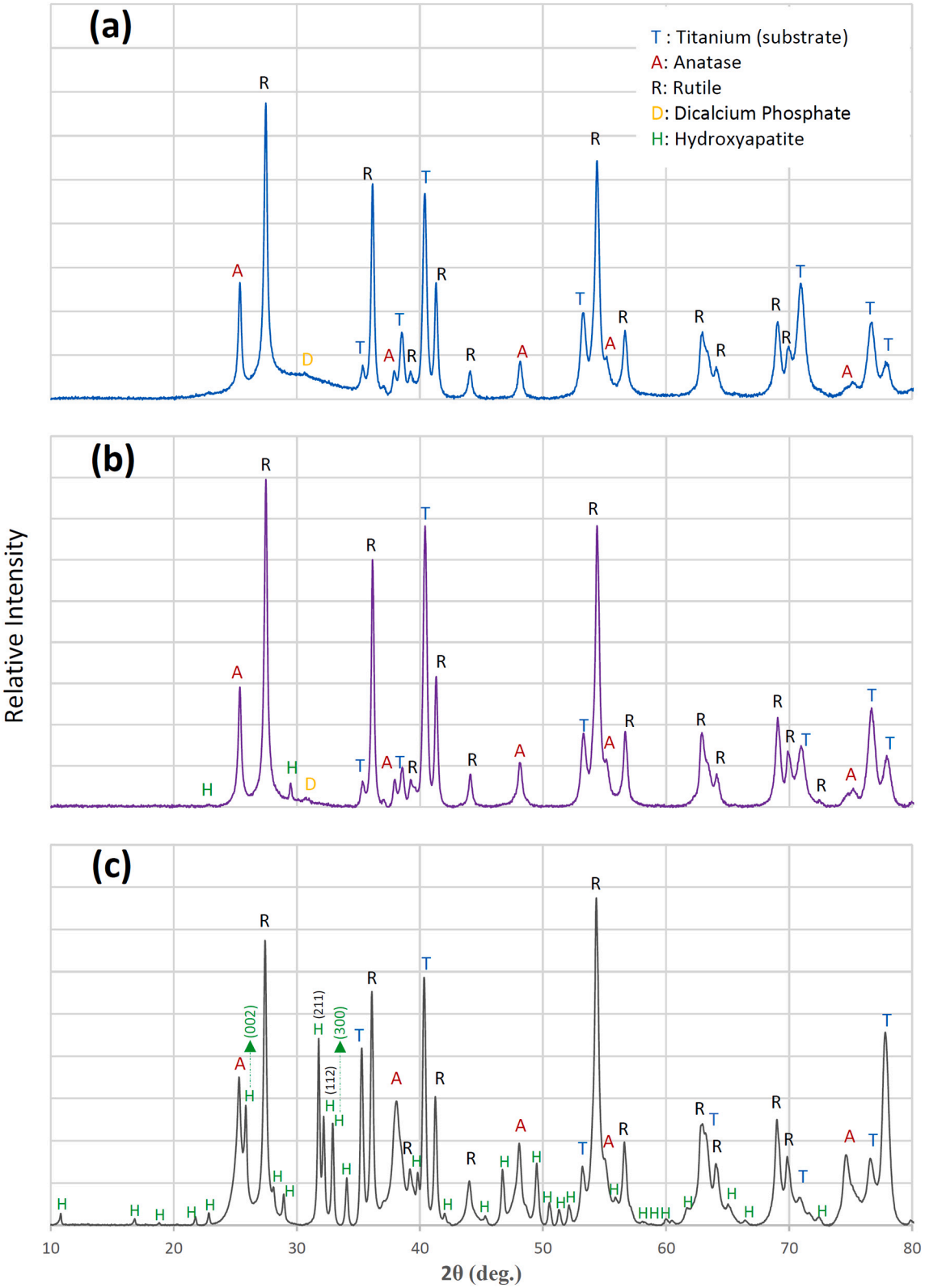

Fig. 3. The XRD patterns of Ag-containing PEO layers (a) before, and after (b) 2 h and (c) 4 h of hydrothermal treatment.

nanoparticles were drawn into the electrolytic plasma and discharge region.

The cross-sectional images showed a relatively uniform thickness of 12–15 μm of the Ag-containing PEO layers (Fig. 2c). The dense inner barrier layer was also found firmly attached to either fully- or partially-molten 3D-printed Ti-6Al-4V particles, illustrating the homogenous growth of the well-adhered oxide layer onto the surface of the geometrically complex porous structure of the SLM specimens.

As revealed by the EDS analysis, the PEO layers contained high Ca/P ratios. However, apart from the diffraction peaks of highly crystalline anatase and rutile TiO_2, the crystalline Ca—P compounds peaks could not be identified (Fig. 3a). The PEO layer was primarily composed of rutile and anatase titanium oxide, and partly of amorphous or low-crystallized Ca—P compounds (2θ = 28–35°). Comparing this pattern with those obtained following hydrothermal treatment (Fig. 3b) revealed the evolution of the crystalline HA during the applied hydrothermal treatment. After 2 h of hydrothermal treatment, an amorphous to the crystalline transition of Ca—P compounds occurred and two sharp peaks corresponding to dicalcium phosphate (D) and hydroxyapatite (H) appeared in the spectrum. This suggests that under the high-temperature and high-pressure steam water, the amorphous phases were dissolved and recrystallized into higher crystalline phases, such as dicalcium phosphate and hydroxyapatite within the PEO layer. As hydrothermal treatment time was extended to 4 h, the characteristic peaks of the (211), (112), and (300) planes of hydroxyapatite turned sharp and distinct, suggesting the presence of highly crystalline HA (Fig. 3c). The higher intensity ratio of (002) to (300) planes, as compared to the standard hydroxyapatite (0.67) confirms the preferential growth of HA crystals from the negatively charged *c*-surfaces [38].

Relative to the PEO-treated surfaces (Fig. 4a), the hydrothermal treatment for 2 h generated additional spindle-like nanofeatures on the surface (Fig. 4b). Further increasing the time of the hydrothermal treatment resulted in a significantly different surface morphology including high aspect ratio needles and pillars outgrown on the surface (Fig. 4c).

The mechanism of the formation of nanocrystalline HA during the hydrothermal treatment of the PEO layers can be explained as follows. The hydrothermal treatment is generally governed by the nucleation

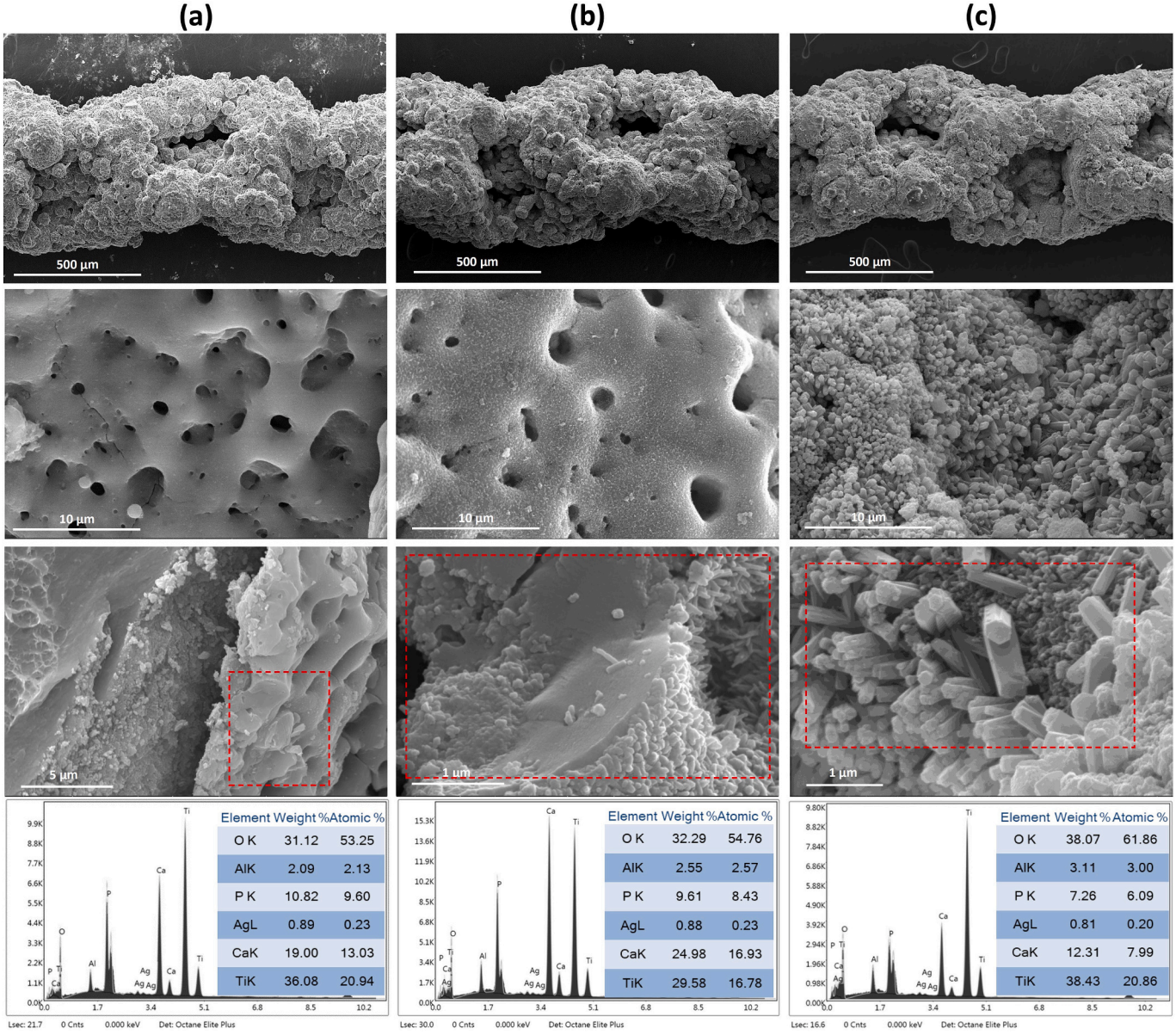

Fig. 4. The FESEM images of the surface morphologies of PEO-treated as-printed implants before (a), and after the subsequent hydrothermal treatment at 250 °C for 2 h (b) and 4 h (c).

and growth of HA crystals [39]. During the nucleation stage, the hydroxyl anions from the environment are adsorbed on the surface. Under a powerful thermodynamic tendency caused by the high-temperature and high-pressure steam water, Ca and P ions within the PEO layer are believed to diffuse toward the surface and interact with the surface-adsorbed OH^- groups [33,40]. The dissolution of the amorphous Ca—P compounds from the outermost surface layer also increases the local supersaturation of Ca and P in the vicinity of the OH^- groups. The formation of HA crystals, therefore, can take place through the following chemical reaction [41]:

$$10Ca^{2+} + 6PO_4^{3-} + 2OH^- \leftrightarrow Ca_{10}(PO_4)_6(OH)_2 \quad (1)$$

This reaction (1) is primarily controlled by the thermodynamic driving force that dictates the nucleation and growth processes. This effect is defined by the variation of Gibbs free energy according to the following equation [42]:

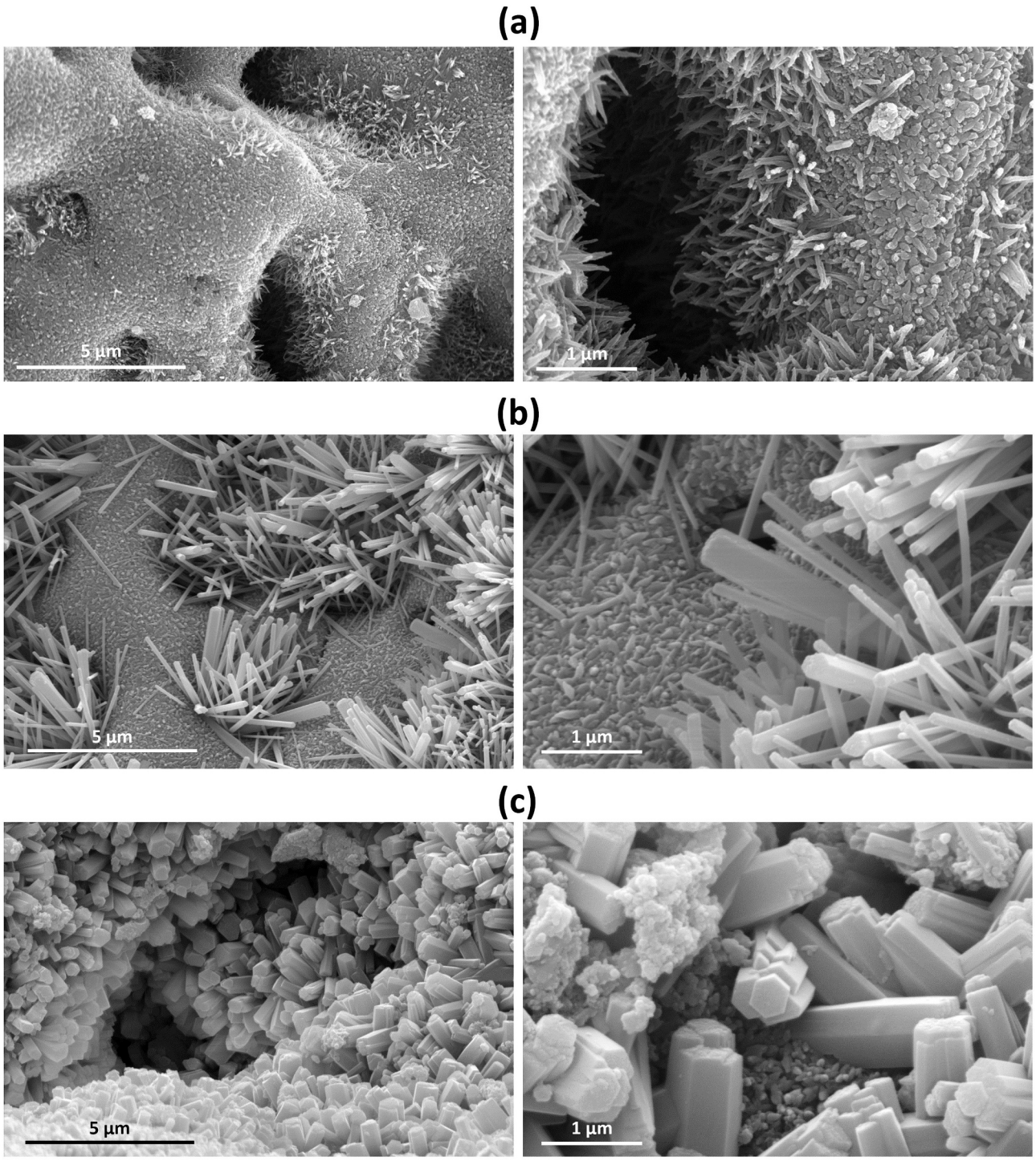

Fig. 5. The formation of HA crystals through hydrothermal treatment at 250 °C: (a) HA needles firstly formed inside the pores (after 2 h), (b) the oriented growth of HA needles along *c*-axis after 3 h and formation of HA nanorods, and (c) the radial growth of hexagonal HA pillars through the parallel arrangement of nanorods. The aggregation of Ca—P particles eroded from HA pillars is visible in (c).

$$\Delta G = \frac{-RT}{n} ln(S) = \frac{-RT}{n} ln\left(\frac{\alpha_A \cdot \alpha_B}{K_{SP}}\right) \quad (2)$$

where R is the universal gas constant (8.314 $J \cdot mol^{-1} \cdot K^{-1}$), T is the reaction temperature (K), n is the number of ions in hydroxyapatite molecule, and S is the supersaturation degree that is defined by the ratio of the activity of ionic species (α_A, α_B, *etc.*) to the solubility constant of the product, K_{sp}.

In the present study, the supersaturation index, SI, can be defined according to Eqs. (1) and (2) as:

$$SI = log(S) = log\left(\frac{\alpha^{10}_{Ca^{2+}} \alpha^{6}_{PO_4^{3-}} \alpha^{2}_{OH^-}}{K_{SP}}\right) \quad (3)$$

The formation of hydroxyapatite crystals of the desired size can, therefore, be explained according to the supersaturation process taking place during the hydrothermal treatment of the PEO layers.

When $SI \leq 0$, there is no thermodynamic driving force for hydroxyapatite formation (*i.e.*, $\Delta G^{HA} \geq 0$). In supersaturated conditions (*i.e.*, $SI > 0$), however, the competition between the nucleation and growth determines the final size, morphology, and distribution of the formed HA crystals. Highly positive SI values indicate the domination of the nucleation process, while for lower supersaturations, the growth of HA crystals prevails the nucleation, and larger crystals are formed.

At the beginning of the hydrothermal treatment, a large amount of Ca and P ions are enriched in the vicinity of the adsorbed OH^- groups at the subsurface of the PEO layer. This locally high supersaturation, which is caused by the ionic diffusion toward the surface can lead to the homogenous formation of spindle-like nanocrystals all over the PEO layer (Fig. 5a). A smaller diffusion distance and higher concentrations of Ca and P ions cause the needles to appear inside the porosities.

On the other hand, the formation of hydroxyapatite is accompanied by the depletion of the reactant ions on the surface, resulting in a remarkable decrease in the supersaturation values. It is well known that there are two types of crystalline facets in hydroxyapatite, namely the positively charged a-surfaces and the negatively charged c-surfaces, the latter of which is the predominant hydroxyapatite crystal growth facet [43]. As the hydrothermal treatment continues, the formed HA nanocrystals tend to grow along the c-axis and form the high aspect-ratio nanorods. This oriented growth is consistent with the results of several previous studies on the hydrothermal synthesis of hydroxyapatite [43,44]. During the growth stage, long nanorods reduce the surface energy by sharing the crystallographic a-surfaces [45]. Through a thermodynamically-driven process, the hexagonal HA pillars were developed from the parallel arrangement of high aspect ratio nanorods (Fig. 5c). After 4 h of treatment, the self-rearrangement phenomena resulted in well-defined hexagonal HA pillars of 200–700 nm in diameter.

3.2. Ion release

Within the first day, 6.6 ± 0.6 ppm of Ca^{2+} was leached from the PEO surfaces into PBS (Fig. 6a). After 7 days, this value reached 15.5 ± 1.2 ppm and continued to slowly increase up to 25.5 ± 2.1 ppm after 28 days. This sustained release of Ca^{2+} from the PEO-treated specimens could be attributed to the high concentration of calcium ions and the easily soluble amorphous structure compounds at the outermost surface of the layer.

The concentration of the released Ca^{2+}, however, decreased after performing a subsequent hydrothermal treatment (Fig. 6a). After hydrothermal treatment for 2 h, this decrease was not significant and a large amount of unreacted dissolved calcium ions was liberated from the surface. This also suggests that the solubility of low-crystalline spindle-like HA nanocrystals is higher [46]. In comparison, the lower rate of release of Ca^{2+} from the PEO-HT4 surfaces indicates a higher degree of crystallinity for the hexagonal HA pillars, which is consistent with what was already discussed based on the results of the XRD analysis. In other words, the PEO layer provides Ca and P for hydroxyapatite formation and growth through the hydrothermal treatment. As the hydrothermal treatment progresses in time, Ca and P ions diffuse toward the outer surface. The unreacted calcium ions can firstly be released into the PBS,

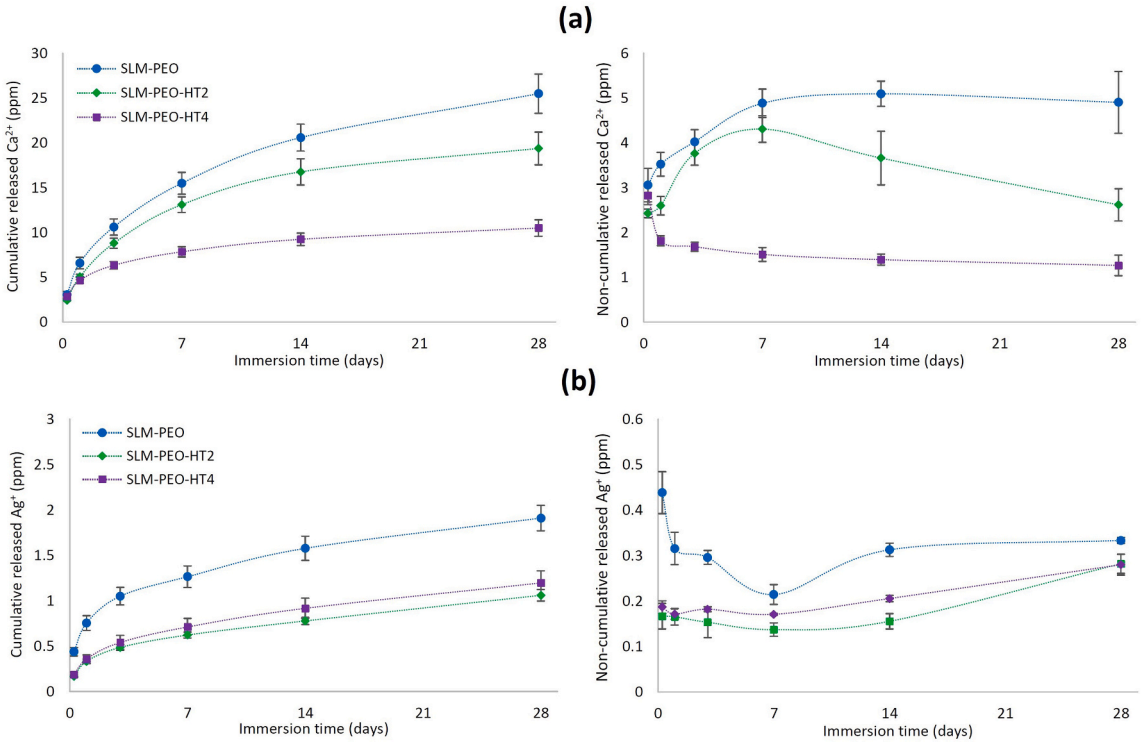

Fig. 6. The non-cumulative (right) and cumulative (left) release profiles of Ca^{2+} (a), and Ag^+ (b) from the surface of PEO- and PEO-HT treated SLM implants during 28 days of immersion in PBS.

but after the first day of immersion, due to the high crystallinity of HA pillars on the surface of PEO-HT4 implants, the non-cumulative release profiles of Ca^{2+} displayed a downward tendency.

The ICP-OES measurements also showed the continued release of Ag^{+} in the leaching profiles of all experimental groups for up to 28 days (Fig. 6b). However, the application of the hydrothermal treatment decreased the total content of the liberated silver ions, especially in the first three days after the start of the immersion test, which could be attributed to the coverage of the surface with HA nanocrystals. Overall, the cumulative release of Ag^{+} from all the experimental groups after 28 days was below the levels that are considered cytotoxic for osteoblasts [15].

3.3. Antimicrobial activity

The metabolic activity of *S. aureus* on PEO layers showed that the incorporation of a trace amount of Ag NPs in the PEO layers significantly (***$p < 0.001$) improved their antibacterial activity (Fig. 7). However, the effects of Ag NPs alone lasted only for up to 8 h. The application of hydrothermal treatment drastically elongated the period within which a strong antibacterial behavior was present to the end of the time duration within which the experiments were performed (*i.e.*, 48 h). A more detailed analysis of the antibacterial behavior of the different groups is presented below.

After 4 and 8 h of culture, the Ag-containing PEO layers revealed a strong bactericidal effect, whereas Ag-free PEO layers did not (Fig. 7). This is consistent with the fact that the oxidation of the embedded Ag NPs results in a locally high concentration of silver ions, which prevents the bacteria from attaching to and colonizing the implant surface particularly at the early time points [15]. Lee and Murphy [47] showed that only 0.2–0.5 ppm of the Ag^{+} concentrations can efficiently suppress the growth of *S. aureus* on Ag NPs-contained CaP coatings. After 24 and 48 h, however, no significant variations ($p > 0.05$) in the levels of bacterial metabolic activity were observed between Ag-free and Ag-containing PEO layers without hydrothermal treatments. The bacteria were found stacked on top of each other and colonized in the form of small clusters (Fig. 8). This indicates that the concentration of the released ions was not high enough to completely prevent the *S. aureus* bacteria from adhering to the surface (Fig. 7). However, the presence of very high concentrations of Ag NPs within the oxide layer might lead to some cytotoxic effects [22,23,25].

The application of the hydrothermal treatment resulted in significantly less viability of bacterial cells for the entire duration of the antibacterial assays. Moreover, while the presence of high doses of Ag NPs within the oxide layer might lead to some cytotoxic effects, our results showed that the application of the post-PEO hydrothermal treatment can modify the surface to impart both cytocompatibility and antibacterial properties. The curves in Fig. 6 showed the sustained release of silver ions from the PEO-HT2 and PEO-HT4 groups, which means that Ag^{+} can diffuse through the hydrothermally formed HA layer and still maintain the antibacterial effect. During the hydrothermal treatment, the embedded Ag NPs may dissolve and release silver ions while interacting with high-temperature, high-pressure water. Therefore, through an ion-exchange reaction with Ca ions, silver has been reported to lodge into the hydroxyapatite crystalline structure [48,49], thereby maintaining the sustained antibacterial leaching activity.

Even though the surface hydrothermal treatment can be applied for intricate 3D macro-porous samples, it is not capable of creating dimensionally uniform nanotopographies. However, the presence of the irregular nanotopographical features on the surface is still believed to make it unfavorable for bacterial adhesion [50].

The combination of nanotopographical features and Ag NPs on the surface, therefore, significantly improved the antibacterial properties of the implants. Both the SLM-PEO-HT2 and SLM-PEO-HT4 groups were found to illustrate the highest antibacterial activity at all the time points, where after 48 h of culture just individual bacteria were separately attached to the surface and no biofilm formation was observed.

3.4. Cell response

The application of the hydrothermal treatments particularly in the PEO-HT2 group resulted in both significantly improved cell proliferation and significantly higher levels of ALP activity (Fig. 9). The MC3T3-E1 cells cultured on the PEO-HT2 surfaces exhibited the highest metabolic activity as compared to both the PEO and PEO-HT4 groups, at all the different time points (Fig. 9a). In addition, the same surfaces resulted in significantly higher levels of ALP activity at both days investigated (Fig. 9b). Imaging of the cells and the surface-cell interface by FESEM at various culturing times (Fig. 10) indicated that the cells could attach and spread after 1 day of culture on all the surfaces. However, at longer times, cells cultured on the PEO-HT2 surfaces followed more uniformly the multi-scale topography and completely covered the 3D-printed

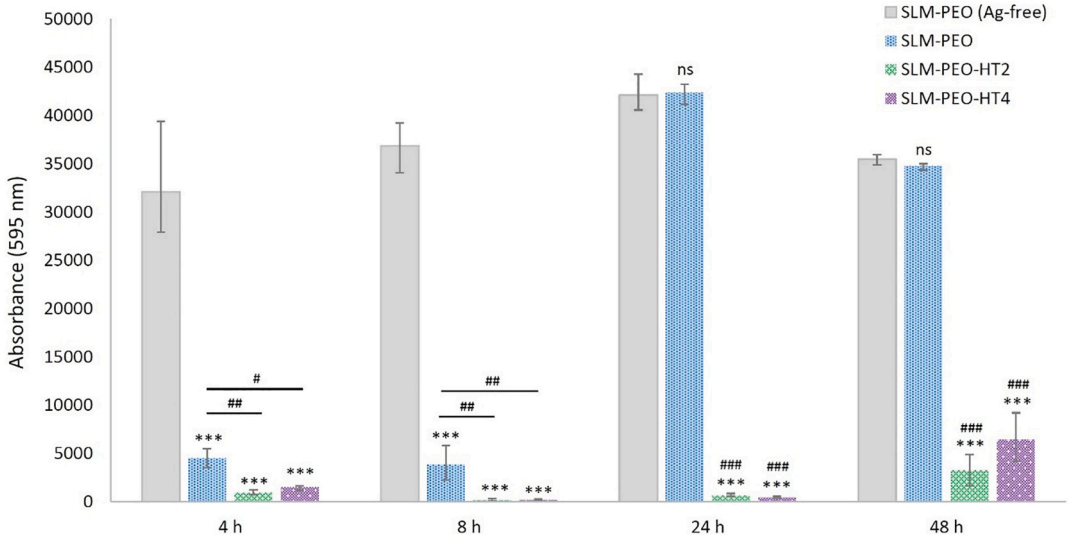

Fig. 7. The results of the PrestoBlue assay for the metabolic activity of *S. aureus* adhered to the surface of biofunctionalized implants after 4, 8, 24, and 48 h of culture. Ag-free PEO layer, fabricated in the same condition as the SLM-PEO group (Ag-containing), showed no antibacterial behavior. Significant differences are indicated by ns=not significant: $p > 0.05$, *$p < 0.05$, **$p < 0.01$, ***$p < 0.001$ compared with SLM-PEO (Ag-free) and $^{\#}p < 0.05$, $^{\#\#}p < 0.01$, $^{\#\#\#}p < 0.001$ compared with Ag-containing SLM-PEO group.

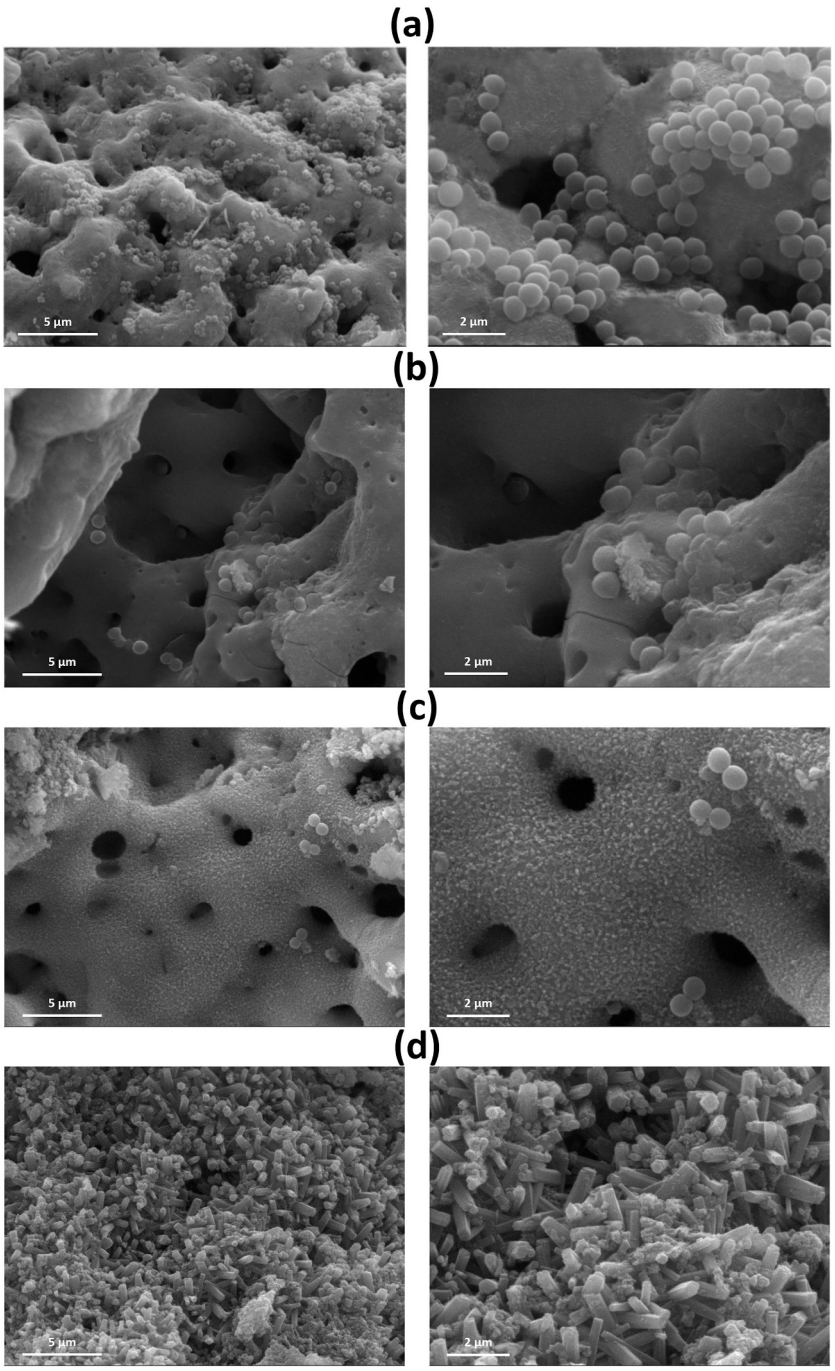

Fig. 8. The SEM images of the *S. aureus* bacteria adhered to the surface of (a) Ag-free SLM-PEO and (b) Ag-containing SLM-PEO, (c) SLM-PEO-HT2, and (d) SLM-PEO-HT4 after 48 h of culture.

macro-porous implant after 14 days. The spindle-like nanocrystals provided a favorable anchorage substrate for cytoplasmic extensions to easily attach and move on the implant surface during the proliferative stage. By comparison, the pillar-like structure of HA crystals on PEO-HT4 surfaces suppressed cell spreading due to their sub-optimal shape and size. These findings indicate that the PEO-HT2 surfaces could stimulate proliferation, migration, and differentiation of these cells.

The ability of the surface to adsorb proteins strongly influences cell adhesion and proliferation. The presence of calcium phosphate compounds on surfaces is believed to improve cell adhesion [51]. It is, however, strongly affected by the surface characteristics, such as surface roughness, surface area, crystallinity, and the solubility of calcium phosphates. In general, protein adhesion is improved for roughness values < 100 nm [52]. The dissolution process of calcium phosphates is also inversely proportional to crystallinity. Highly crystalline calcium phosphates show low solubility, low ion exchange, and, thus, slow rates of recrystallization, whereas amorphous or low crystalline calcium phosphates are highly soluble, thereby stimulating effective protein adhesion and bone regeneration [53].

Application of 2 h of hydrothermal treatment on PEO treated implants provided a large surface area by creating spindle-like HA nanocrystals within the microporous structure of the PEO layer. The presence of nanoscale features based on calcium phosphate chemistry is considered beneficial for enhancing proteins adsorption and cell adhesion [54]. Therefore, the formation of HA nanoscale features (30–80 nm in diameter and 100–150 nm in length) is considered a favorable factor

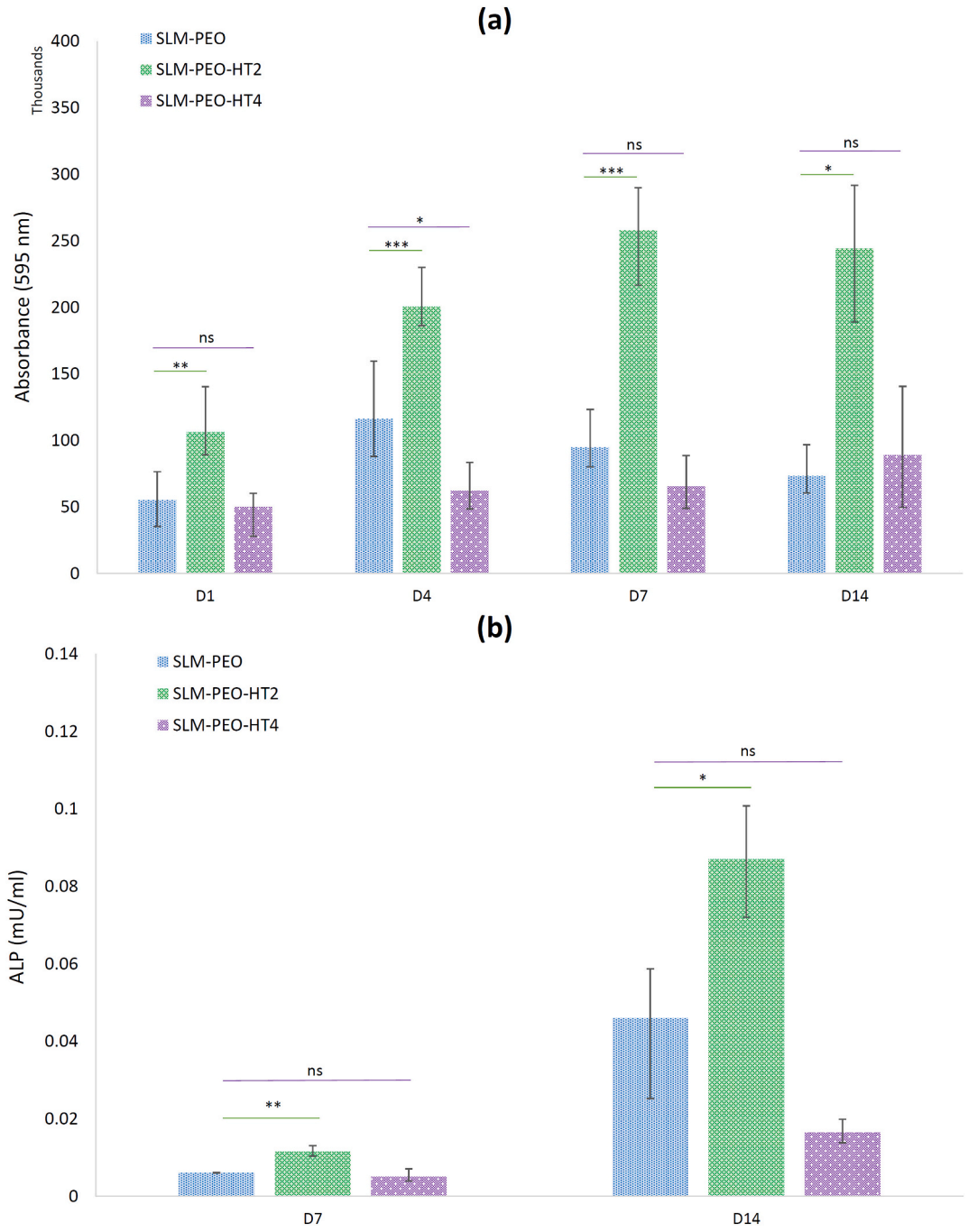

Fig. 9. (a) The metabolic activity of MC3T3-E1 cells on the PEO- and PEO-HT treated SLM implants. (b) The osteogenic differentiation of MC3T3-E1 cells on the three different types of biofunctionalized implants. Significant differences are indicated by $*p < 0.05$, $**p < 0.01$, $***p < 0.001$.

contributing to the enhanced cellular response observed, which is in line with the findings of other studies [45,55–57]. In addition to the nano-features, it has been shown that the presence of micropores in the structure of the PEO layer plays a major role in providing an osteo-conductive surface [26]. As the microporous structure was not affected in the PEO-HT2 specimens (Fig. 4), their unique hierarchical micro-nano structure is likely to show the best cell response. In addition to the physical properties and topographical features, the osteogenic behavior is strongly influenced by surface chemistry, where the release of optimum amounts of Ca and P ions from the implant surface is expected to promote osteogenic differentiation. It has been reported that the lower crystalline calcium phosphate is more favorable for osteogenic differentiation [58]. Hu et al. [59] also suggested that the effects of hydroxyapatite crystallite size should be taken into account, where the smaller nanocrystallites resulted in higher levels of ALP activity. Meanwhile, it is also well known that the solubility of hydroxyapatite is inversely related to its crystallinity [60]. Therefore, the highly crystalline HA pillars on PEO-HT4 implants, which were barely soluble in the microenvironment, could have contributed to the lower ALP activity measured.

In summary, the decoration of the microporous PEO layers with uniformly distributed spindle-like HA nanocrystals not only revealed a hierarchical structure that facilitated the proliferation and osteogenic differentiation of preosteoblasts on the macro-porous SLM implants but also provided the highest degree of bactericidal properties afforded by the addition of silver nanoparticles.

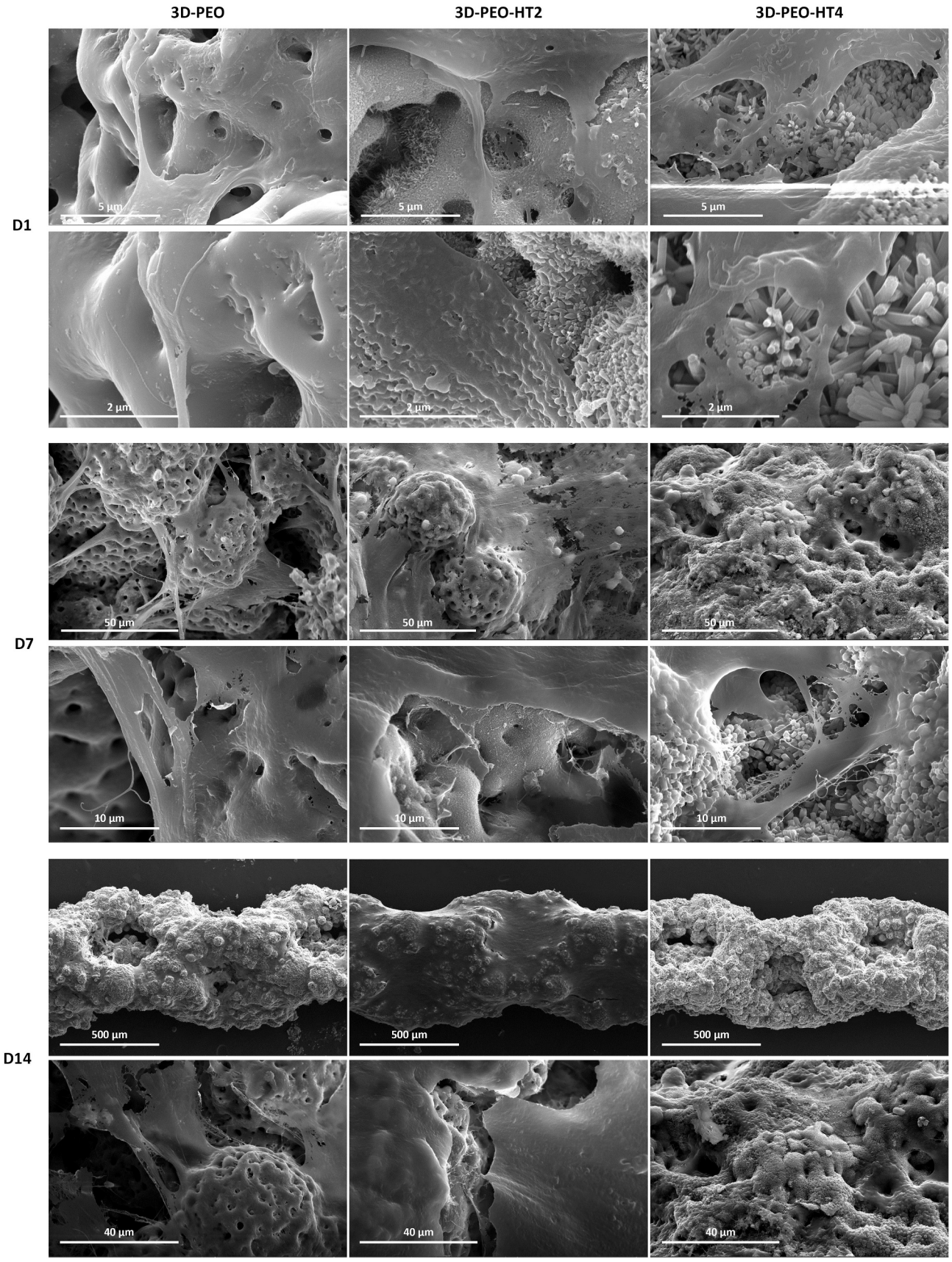

Fig. 10. The FESEM images of the MC3T3-E1 cells on the SLM-PEO, SLM-PEO-HT2, and SLM-PEO-HT4 groups after 1, 7, and 14 days of cell culture. After 14 days, the porous structure of SLM-PEO-HT2 implants was completely covered with cells.

4. Conclusions

To develop multifunctional layers on additively manufactured Ti-6Al-4V implants, a hierarchically structured surface including an interconnected microporous TiO_2 layer containing silver nanoparticles and hydroxyapatite nanocrystals was synthesized through plasma electrolytic oxidation followed by hydrothermal treatment. According to the supersaturation of Ca and P ions at the outermost surface of PEO layers, two different morphologies of hydroxyapatite, namely nano-spindles and nano-pillars, were produced by altering the time of the hydrothermal treatment.

Even though the application of the hydrothermal treatment decreased the total content of the released silver ions, the presence of the hydrothermally formed nanotopographical features on PEO-HT2 and PEO-HT4 surfaces led to significantly less viability of the bacterial cells for the entire duration of the antibacterial assays.

The pillar-like structure of the HA nanocrystals present on the PEO-HT4 surfaces, however, suppressed cell spreading due to their sub-optimal shape and size. The spindle-like HA nanocrystals induced by PEO-HT2 decorated the microporous surface and stimulated the osteogenic differentiation of pre-osteoblasts, leading to a multifunctional surface with enhanced bioactivity for titanium bone implants.

CRediT authorship contribution statement

Mohammad Fazel	Conceptualization, Investigation, Methodology, Writing, Review & editing
Hamid Reza Salimijazi	Conceptualization, Methodology, Resources, Review & editing, Supervision
Morteza Shamanian	Conceptualization, Methodology, Resources, Review & editing, Supervision
Michelle Minneboo	Investigation, Methodology
Khashayar Modaresifar	Investigation, Methodology
Ingmar van Hengel	Investigation, Methodology
Lidy Fratila-Apachitei	Conceptualization, Methodology, Resources, Review & editing, Supervision
Iulian Apachitei	Conceptualization, Methodology, Resources, Review & editing, Supervision
Amir Abbas Zadpoor	Conceptualization, Methodology, Resources, Review & editing, Supervision

Declaration of competing interest

The authors declare that they have no known competing financial interests or personal relationships that could have appeared to influence the work reported in this paper.

Acknowledgment

The authors are grateful to Dr. C.W. Hagen from the Department of Imaging Physics (TU Delft) for providing access to the SEM equipment.

References

[1] I.-J. Hwang, H.-C. Choe, Hydroxyapatite coatings containing Zn and Si on Ti-6Al-4Valloy by plasma electrolytic oxidation, Appl. Surf. Sci. 432 (2018) 337–346.
[2] M. Fazel, H.R. Salimijazi, M.A. Golozar, M.R. Garsivaz jazi, A comparison of corrosion, tribocorrosion and electrochemical impedance properties of pure Ti and Ti6Al4V alloy treated by micro-arc oxidation process, Appl. Surf. Sci. 324 (2015) 751–756.
[3] G. Ryan, A. Pandit, D.P. Apatsidis, Fabrication methods of porous metals for use in orthopaedic applications, Biomaterials 27 (13) (2006) 2651–2670.
[4] J. Karbowniczek, F. Muhaffel, G. Cempura, H. Cimenoglu, A. Czyrska-Filemonowicz, Influence of electrolyte composition on microstructure, adhesion and bioactivity of micro-arc oxidation coatings produced on biomedical Ti6Al7Nb alloy, Surf. Coat. Technol. 321 (2017) 97–107.
[5] Z. Gorgin Karaji, R. Hedayati, B. Pouran, I. Apachitei, A.A. Zadpoor, Effects of plasma electrolytic oxidation process on the mechanical properties of additively manufactured porous biomaterials, Mater. Sci. Eng. C 76 (2017) 406–416.
[6] A. Vance, K. Bari, A. Arjunan, Compressive performance of an arbitrary stiffness matched anatomical Ti64 implant manufactured using Direct Metal Laser Sintering, Mater. Des. 160 (2018) 1281–1294.
[7] M. Ridzwan, S. Shuib, Problem of stress shielding and improvement to the hip implant designs: a review, Journal of Medical Sciences 7 (2007) 460–467.
[8] L.E. Murr, S.M. Gaytan, D.A. Ramirez, E. Martinez, J. Hernandez, K.N. Amato, P. W. Shindo, F.R. Medina, R.B. Wicker, Metal fabrication by additive manufacturing using laser and electron beam melting technologies, J. Mater. Sci. Technol. 28 (1) (2012) 1–14.
[9] H.M.A. Kolken, S. Janbaz, S.M.A. Leeflang, K. Lietaert, H.H. Weinans, A. A. Zadpoor, Rationally designed meta-implants: a combination of auxetic and conventional meta-biomaterials, Mater. Horiz. 5 (1) (2018) 28–35.
[10] M.J. Song, D. Dean, M.L. Knothe Tate, Mechanical modulation of nascent stem cell lineage commitment in tissue engineering scaffolds, Biomaterials 34 (23) (2013) 5766–5775.
[11] X.-Y. Zhang, G. Fang, S. Leeflang, A.A. Zadpoor, J. Zhou, Topological design, permeability and mechanical behavior of additively manufactured functionally graded porous metallic biomaterials, Acta Biomater. 84 (2019) 437–452.
[12] S. Van Bael, Y.C. Chai, S. Truscello, M. Moesen, G. Kerckhofs, H. Van Oosterwyck, J.P. Kruth, J. Schrooten, The effect of pore geometry on the in vitro biological behavior of human periosteum-derived cells seeded on selective laser-melted Ti6Al4V bone scaffolds, Acta Biomater. 8 (7) (2012) 2824–2834.
[13] S.M. Ahmadi, R. Hedayati, Y. Li, K. Lietaert, N. Tümer, A. Fatemi, C.D. Rans, B. Pouran, H. Weinans, A.A. Zadpoor, Fatigue performance of additively manufactured meta-biomaterials: the effects of topology and material type, Acta Biomater. 65 (2018) 292–304.
[14] S. Zhao, S.J. Li, W.T. Hou, Y.L. Hao, R. Yang, L.E. Murr, Microstructure and mechanical properties of open cellular Ti–6Al–4V prototypes fabricated by electron beam melting for biomedical applications, Mater. Technol. 31 (2) (2016) 98–107.
[15] I.A.J. van Hengel, M. Riool, L.E. Fratila-Apachitei, J. Witte-Bouma, E. Farrell, A. A. Zadpoor, S.A.J. Zaat, I. Apachitei, Selective laser melting porous metallic implants with immobilized silver nanoparticles kill and prevent biofilm formation by methicillin-resistant Staphylococcus aureus, Biomaterials 140 (2017) 1–15.
[16] D.J. Yoo, Porous scaffold design using the distance field and triply periodic minimal surface models, Biomaterials 32 (31) (2011) 7741–7754.
[17] A. Santos-Coquillat, R. Gonzalez Tenorio, M. Mohedano, E. Martinez-Campos, R. Arrabal, E. Matykina, Tailoring of antibacterial and osteogenic properties of Ti6Al4V by plasma electrolytic oxidation, Appl. Surf. Sci. 454 (2018) 157–172.
[18] S. Amin Yavari, R. Wauthle, A.J. Böttger, J. Schrooten, H. Weinans, A.A. Zadpoor, Crystal structure and nanotopographical features on the surface of heat-treated and anodized porous titanium biomaterials produced using selective laser melting, Appl. Surf. Sci. 290 (2014) 287–294.
[19] A.G. Gristina, P.T. Naylor, Q.N. Myrvik, Biomaterial-centered infections: microbial adhesion versus tissue integration, in: T. Wadström, I. Eliasson, I. Holder, Å. Ljungh (Eds.), Pathogenesis of Wound and Biomaterial-Associated Infections, Springer London, London, 1990, pp. 193–216.
[20] G. Subbiahdoss, R. Kuijer, D.W. Grijpma, Microbial biofilm growth vs. tissue integration: "the race for the surface" experimentally studied, Acta Biomaterialia 5 (5) (2009) 1399–1404.
[21] R. Jones, R. Draheim, M. Roldo, Silver nanowires: synthesis, antibacterial activity and biomedical applications, Appl. Sci. 8 (5) (2018) 673.
[22] S. Amin Yavari, L. Loozen, F.L. Paganelli, S. Bakhshandeh, K. Lietaert, J.A. Groot, A.C. Fluit, C.H.E. Boel, J. Alblas, H.C. Vogely, H. Weinans, A.A. Zadpoor, Antibacterial behavior of additively manufactured porous titanium with nanotubular surfaces releasing silver ions, ACS Appl. Mater. Interfaces 8 (27) (2016) 17080–17089.
[23] M. Croes, S. Bakhshandeh, I.A.J. van Hengel, K. Lietaert, K.P.M. van Kessel, B. Pouran, B.C.H. van der Wal, H.C. Vogely, W. Van Hecke, A.C. Fluit, C.H.E. Boel, J. Alblas, A.A. Zadpoor, H. Weinans, S. Amin Yavari, Antibacterial and immunogenic behavior of silver coatings on additively manufactured porous titanium, Acta Biomater. 81 (2018) 315–327.
[24] A. Ivask, A. ElBadawy, C. Kaweeteerawat, D. Boren, H. Fischer, Z. Ji, C.H. Chang, R. Liu, T. Tolaymat, D. Telesca, J.I. Zink, Y. Cohen, P.A. Holden, H.A. Godwin, Toxicity mechanisms in Escherichia coli vary for silver nanoparticles and differ from ionic silver, ACS Nano 8 (1) (2014) 374–386.
[25] B.S. Necula, J.P.T.M. van Leeuwen, L.E. Fratila-Apachitei, S.A.J. Zaat, I. Apachitei, J. Duszczyk, In vitro cytotoxicity evaluation of porous TiO2–Ag antibacterial coatings for human fetal osteoblasts, Acta Biomater. 8 (11) (2012) 4191–4197.
[26] P. Xiu, Z. Jia, J. Lv, C. Yin, Y. Cheng, K. Zhang, C. Song, H. Leng, Y. Zheng, H. Cai, Z. Liu, Tailored surface treatment of 3D printed porous Ti6Al4V by microarc oxidation for enhanced osseointegration via optimized bone in-growth patterns and interlocked bone/implant interface, ACS Appl. Mater. Interfaces 8 (28) (2016) 17964–17975.
[27] Y. Yan, J. Sun, Y. Han, D. Li, K. Cui, Microstructure and bioactivity of Ca, P and Sr doped TiO2 coating formed on porous titanium by micro-arc oxidation, Surf. Coat. Technol. 205 (6) (2010) 1702–1713.
[28] Q. Li, W. Yang, C. Liu, D. Wang, J. Liang, Correlations between the growth mechanism and properties of micro-arc oxidation coatings on titanium alloy: effects of electrolytes, Surf. Coat. Technol. 316 (2017) 162–170.
[29] V.M. Frauchiger, F. Schlottig, B. Gasser, M. Textor, Anodic plasma-chemical treatment of CP titanium surfaces for biomedical applications, Biomaterials 25 (4) (2004) 593–606.
[30] S.A. Yavari, B.S. Necula, L.E. Fratila-Apachitei, J. Duszczyk, I. Apachitei, Biofunctional surfaces by plasma electrolytic oxidation on titanium biomedical alloys, Surf. Eng. 32 (6) (2016) 411–417.

[31] I.d.S.V. Marques, N.C. da Cruz, R. Landers, J.C.-C. Yuan, M.F. Mesquita, C. Sukotjo, M.T. Mathew, V.A.R. Barão, Incorporation of Ca, P, and Si on bioactive coatings produced by plasma electrolytic oxidation: the role of electrolyte concentration and treatment duration, Biointerphases 10(4) (2015) 041002–11.
[32] L. Bai, Z. Du, J. Du, W. Yao, J. Zhang, Z. Weng, S. Liu, Y. Zhao, Y. Liu, X. Zhang, X. Huang, X. Yao, R. Crawford, R. Hang, D. Huang, B. Tang, Y. Xiao, A multifaceted coating on titanium dictates osteoimmunomodulation and osteo/angio-genesis towards ameliorative osseointegration, Biomaterials 162 (2018) 154–169.
[33] L. Chang, L. Tian, W. Liu, X. Duan, Formation of dicalcium phosphate dihydrate on magnesium alloy by micro-arc oxidation coupled with hydrothermal treatment, Corros. Sci. 72 (2013) 118–124.
[34] M. Ganjian, K. Modaresifar, M.R.O. Ligeon, L.B. Kunkels, N. Tümer, L. Angeloni, C. W. Hagen, L.G. Otten, P.-L. Hagedoorn, I. Apachitei, L.E. Fratila-Apachitei, A. A. Zadpoor, Nature helps: toward bioinspired bactericidal nanopatterns, Adv. Mater. Interfaces 6 (16) (2019) 1900640.
[35] D. Berrington, Viability reagent, prestoblue, in comparison with other available reagents, utilized in cytotoxicity and antimicrobial assays, International Journal of Microbiology 2013, 2013.
[36] F. Simchen, M. Sieber, T. Lampke, Electrolyte influence on ignition of plasma electrolytic oxidation processes on light metals, Surface and Coatings Technology 315 (Supplement C) (2017) 205–213.
[37] R.O. Hussein, X. Nie, D.O. Northwood, A. Yerokhin, A. Matthews, Spectroscopic study of electrolytic plasma and discharging behaviour during the plasma electrolytic oxidation (PEO) process, J. Phys. D. Appl. Phys. 43 (10) (2010) 105203.
[38] M.-A. Faghihi-Sani, A. Arbabi, A. Mehdinezhad-Roshan, Crystallization of hydroxyapatite during hydrothermal treatment on amorphous calcium phosphate layer coated by PEO technique, Ceram. Int. 39 (2) (2013) 1793–1798.
[39] C. Yang, K. Lin, J. Chang, A simple way to synthesize 3D hierarchical HAp porous microspheres with sustained drug release, Ceramics International 41 (9, Part A) (2015) 11153–11160.
[40] M. Fazel, H.R. Salimijazi, M. Shamanian, I. Apachitei, A.A. Zadpoor, Influence of hydrothermal treatment on the surface characteristics and electrochemical behavior of Ti-6Al-4V bio-functionalized through plasma electrolytic oxidation, Surf. Coat. Technol. 374 (2019) 222–231.
[41] H. Farnoush, F. Muhaffel, H. Cimenoglu, Fabrication and characterization of nano-HA-45S5 bioglass composite coatings on calcium-phosphate containing micro-arc oxidized CP-Ti substrates, Appl. Surf. Sci. 324 (2015) 765–774.
[42] Y. Yang, Q. Wu, M. Wang, J. Long, Z. Mao, X. Chen, Hydrothermal synthesis of hydroxyapatite with different morphologies: influence of supersaturation of the reaction system, Cryst. Growth Des. 14 (9) (2014) 4864–4871.
[43] C. Chen, Z. Huang, W. Yuan, J. Li, X. Cheng, R.-a. Chi, Pressure effecting on morphology of hydroxyapatite crystals in homogeneous system, CrystEngComm 13 (5) (2011) 1632–1637.
[44] X. Liu, K. Lin, J. Chang, Modulation of hydroxyapatite crystals formed from α-tricalcium phosphate by surfactant-free hydrothermal exchange, CrystEngComm 13 (6) (2011) 1959–1965.
[45] D.O. Costa, S.J. Dixon, A.S. Rizkalla, One- and three-dimensional growth of hydroxyapatite nanowires during sol–gel–hydrothermal synthesis, ACS Appl. Mater. Interfaces 4 (3) (2012) 1490–1499.
[46] L. Bai, Y. Liu, Z. Du, Z. Weng, W. Yao, X. Zhang, X. Huang, X. Yao, R. Crawford, R. Hang, D. Huang, B. Tang, Y. Xiao, Differential effect of hydroxyapatite nano-particle versus nano-rod decorated titanium micro-surface on osseointegration, Acta Biomater. 76 (2018) 344–358.
[47] J.S. Lee, W.L. Murphy, Functionalizing calcium phosphate biomaterials with antibacterial silver particles, Adv. Mater. 25 (8) (2013) 1173–1179.
[48] Y. Ghani, M.J. Coathup, K.A. Hing, G.W. Blunn, Development of a hydroxyapatite coating containing silver for the prevention of peri-prosthetic infection, J. Orthop. Res. 30 (3) (2012) 356–363.
[49] M. Chimutengwende-Gordon, C. Pendegrass, R. Bayston, G. Blunn, Preventing infection of osseointegrated transcutaneous implants: incorporation of silver into preconditioned fibronectin-functionalized hydroxyapatite coatings suppresses Staphylococcus aureus colonization while promoting viable fibroblast growth in vitro, Biointerphases 9 (3) (2014), 031010.
[50] K. Kapat, P.P. Maity, A.P. Rameshbabu, P.K. Srivas, P. Majumdar, S. Dhara, Simultaneous hydrothermal bioactivation with nano-topographic modulation of porous titanium alloys towards enhanced osteogenic and antimicrobial responses, J. Mater. Chem. B 6 (18) (2018) 2877–2893.
[51] F.S.L. Bobbert, A.A. Zadpoor, Effects of bone substitute architecture and surface properties on cell response, angiogenesis, and structure of new bone, J. Mater. Chem. B 5 (31) (2017) 6175–6192.
[52] E.A. dos Santos, M. Farina, G.A. Soares, K. Anselme, Surface energy of hydroxyapatite and β-tricalcium phosphate ceramics driving serum protein adsorption and osteoblast adhesion, J. Mater. Sci. Mater. Med. 19 (6) (2008) 2307–2316.
[53] L. Xia, Y. Xie, B. Fang, X. Wang, K. Lin, In situ modulation of crystallinity and nano-structures to enhance the stability and osseointegration of hydroxyapatite coatings on Ti-6Al-4V implants, Chem. Eng. J. 347 (2018) 711–720.
[54] J. Jeong, J.H. Kim, J.H. Shim, N.S. Hwang, C.Y. Heo, Bioactive calcium phosphate materials and applications in bone regeneration, Biomater. Res. 23 (2019) 4.
[55] S. Amin Yavari, J. van der Stok, Y.C. Chai, R. Wauthle, Z. Tahmasebi Birgani, P. Habibovic, M. Mulier, J. Schrooten, H. Weinans, A.A. Zadpoor, Bone regeneration performance of surface-treated porous titanium, Biomaterials 35 (24) (2014) 6172–6181.
[56] H. Zhou, J. Lee, Nanoscale hydroxyapatite particles for bone tissue engineering, Acta Biomater. 7 (7) (2011) 2769–2781.
[57] S. Amin Yavari, Y.C. Chai, A.J. Böttger, R. Wauthle, J. Schrooten, H. Weinans, A. A. Zadpoor, Effects of anodizing parameters and heat treatment on nanotopographical features, bioactivity, and cell culture response of additively manufactured porous titanium, Mater. Sci. Eng. C 51 (2015) 132–138.
[58] L. Chou, B. Marek, W.R. Wagner, Effects of hydroxylapatite coating crystallinity on biosolubility, cell attachment efficiency and proliferation in vitro, Biomaterials 20 (10) (1999) 977–985.
[59] Q. Hu, Z. Tan, Y. Liu, J. Tao, Y. Cai, M. Zhang, H. Pan, X. Xu, R. Tang, Effect of crystallinity of calcium phosphate nanoparticles on adhesion, proliferation, and differentiation of bone marrow mesenchymal stem cells, J. Mater. Chem. 17 (44) (2007) 4690–4698.
[60] S.S. Andrea Ruffini, Lorenzo Preti, Anna Tampieri, Synthesis of nanostructured hydroxyapatite via controlled hydrothermal route, in: M. Barbeck (Ed.), Biomaterial-supported Tissue Reconstruction or Regeneration, University Medical Center Hamburg- Eppendorf, 2019.